



Berg Huettenmaenn Monatsh Vol. 168 (5): 239–246
<https://doi.org/10.1007/s00501-023-01353-4>
© The Author(s) 2023

BHM Berg- und
Hüttenmännische
Monatshefte

Influence of Laser Power and Scan Speed on the Formation of Hot Cracks during the Processing of High-speed Steel HS2-2-2 by Laser Powder Bed Fusion

Tim Gerrit Lücke¹, Luke Schüller¹, Andreas Vogelpoth¹, Thomas Laag¹, Jasmin Saewe¹, and Constantin Leon Häfner^{1,2}

¹Fraunhofer ILT, Aachen, Germany

²Chair for Laser Technology LLT, RWTH Aachen University, Aachen, Germany

Received March 9, 2023; accepted April 18, 2023

Abstract: The manufacturing of high-speed steel (HSS) components using the laser powder bed fusion (LPBF) process could create an unprecedented combination of the materials' mechanical properties and the design freedom enabled by the process to unlock new applications, such as milling heads with functionally optimized cooling channels. However, the processing of HSS with the LPBF process shows high susceptibility to cracking. This contribution aims to reduce hot cracking for the processing of HS2-2-2 by investigating the influences of preheating temperature, laser power, and scan speed on the formation of hot cracks. The density and melt pool geometry of the produced parts are measured to further examine the relationship between the processing conditions and the resulting properties. The influence of various process parameters on the formation of hot cracks can be demonstrated. Further investigation shows a relation between hot cracking and the melt pool geometry. With a narrow and shallow melt pool, influenced by laser power and scan speed, the number of hot cracks can be reduced.

Keywords: LPBF, Laser Powder Bed Fusion, SLM, Selective Laser Melting, High-speed steel, Tool steel, High carbon content steel, Hot cracking

Einfluss von Laserleistung und Scangeschwindigkeit auf die Bildung von Heißrissen bei der Verarbeitung von Schnellarbeitsstahl HS2-2-2 mittels Laser Powder Bed Fusion

Zusammenfassung: Die Herstellung von Bauteilen aus Schnellarbeitsstahl (HSS) mit dem Laser Powder Bed Fusion (LPBF) Verfahren könnte eine noch nie dagewesene Kombination aus den mechanischen Eigenschaften des Werkstoffs und der durch das Verfahren ermöglichten Designfreiheit schaffen, die neue Anwendungen wie Fräsköpfe mit funktionsoptimierten Kühlkanälen ermöglicht. Die Verarbeitung von HSS mithilfe des LPBF-Verfahrens ist jedoch aufgrund einer hohen Anfälligkeit für Risse problematisch. Ziel dieser Studie ist es, die Heißrissbildung bei der Verarbeitung von HS2-2-2 zu reduzieren, indem der Einfluss von Vorheiztemperatur, Laserleistung und Scangeschwindigkeit auf die Bildung von Heißrissen untersucht wird. Die Dichte und die Schmelzbadgeometrie der hergestellten Teile werden gemessen, um den Zusammenhang zwischen den Prozessbedingungen und den resultierenden Eigenschaften weiter zu untersuchen. Der Einfluss verschiedener Prozessparameter auf die Bildung von Heißrissen kann nachgewiesen werden. Weitere Untersuchungen zeigen einen Zusammenhang zwischen der Heißrissbildung und der Schmelzbadgeometrie. Mit einem schmalen und flachen Schmelzbad, das von der Laserleistung und der Scangeschwindigkeit beeinflusst wird, kann die Anzahl der Heißrisse reduziert werden.

Schlüsselwörter: LPBF, Laser Powder Bed Fusion, SLM,

T. G. Lücke (✉)
Fraunhofer ILT,
Steinbachstraße 15,
52074 Aachen, Germany
tim.gerrit.luecke@ilt.fraunhofer.de

Selective Laser Melting, Schnellarbeitsstahl, Werkzeugstahl, Stahl mit hohem Kohlenstoffgehalt, Heißrissbildung

1. Introduction

Laser Powder Bed Fusion (LPBF), also known as Selective Laser Melting (SLM), is an additive manufacturing process that is used in industries, such as aerospace, automotive, and medical. In the LPBF process, a metal powder material is applied in thin layers to a substrate plate and then selectively melted using a focused laser beam, resulting in a three-dimensional component. Compared to subtractive processes such as turning and milling, the LPBF process allows greater design freedom without the use of wear tools but also enables the manufacturing of lightweight structures such as lattices. In addition, additive manufacturing can be used to extend the lifespan of certain components by incorporating cooling channel structures into the component [1, 2].

The processing of tool steels with the LPBF process is an active research topic. These steels are characterized primarily by their high hardness and good wear properties and are therefore used primarily in the field of e.g. tool or mould applications [3]. However, only a few tool steels have been qualified for the LPBF process so far. The most common tool steels in LPBF include hot work steels like 1.2709, AISI H11 (1.2343), and AISI H13 (1.2344). Also, high-speed steels with higher carbon content, such as AISI M50 (1.3325) or HS6-3-5-8 (1.3294) can be processed additively [3–6].

However, the alloying concepts and the associated microstructures of these steels favor the formation of cracks [3]. For example, cold cracks can form when a manufactured part cools below its solidus temperature. Internal stresses, triggered by the formation of carbides or brittle phases such as martensite, exceed the local material properties and cause cracking [7, 8]. Such cold cracks can be suppressed with the help of a build plate preheating system [9]. In addition to cold cracks, hot cracks can also occur mostly as transcrystalline defects at temperatures between the solidus and liquidus temperature [7]. Hot cracks can be divided into re-melting cracks (RC), solidification cracks (SC), and ductility dip cracks (DDC). RC mostly occur due to stresses during the solidification of low-melting regions in the underlying layers that are reheated when the new layer is melted [10]. SC are formed during solidification shrinkage of low-melting alloying elements at the crystallization front and form at the rounded dendrite tips [8, 11, 12]. DDC is formed by brittle microstructural components, such as martensite or carbides, which are not remelted during exposure. This reduces the ductility of the microstructure, which can lead to stresses [12].

This contribution focuses on the formation of hot cracks in specimens made with LPBF of high-speed steel HS2-2-2, also known as 1.3294 or ASP®2012, with 0.6 wt.-% carbon content. For this purpose, the influences of laser power (P_L), scan speed (v_s), layer height (H_L), hatch distance (y_s), and build plate preheating temperature (BPPT) on the formation of hot cracks are evaluated. Additionally, the density, melt pool geometry, and hot cracks of the produced specimens are measured to further examine the relationship between the processing conditions and the resulting properties.

2. Materials and Methods

Within the scope of this study, the high-speed steel HS2-2-2 is used. HS2-2-2 is a cobalt-free high-speed steel that displays high toughness up to a hardness of 58 HRC in cold, warm, and hot applications. Applications for this steel include cold working dies, plastic injection molders and dies for extrusion, forging, and hot forming. The chemical composition of the powder material as specified by the manufacturer Erasteel GmbH is displayed in Table 1 [13].

All experiments conducted within the scope of this contribution were performed on a laboratory-scale LPBF machine (Aconity Midi) from Aconity3D GmbH, Germany. The machine is equipped with an Ytterbium fiber laser from Rofin-Sinar Laser GmbH, Germany, with a wavelength of 1070 nm and a maximum power output of 400 W. The circular laser spot with an 80 μm diameter ($1/e^2$) in the focal plane has a gaussian intensity distribution. The machine is furthermore equipped with a 3D scan system from Scanlab GmbH, Germany (varioSCAN40 and intelliSCAN20) and a resistive preheating system, that can heat the base plate to 800 °C. All experiments were carried out under an argon inert gas atmosphere with an oxygen content below 200 ppm with approx. 50 mbar overpressure to the ambient atmosphere.

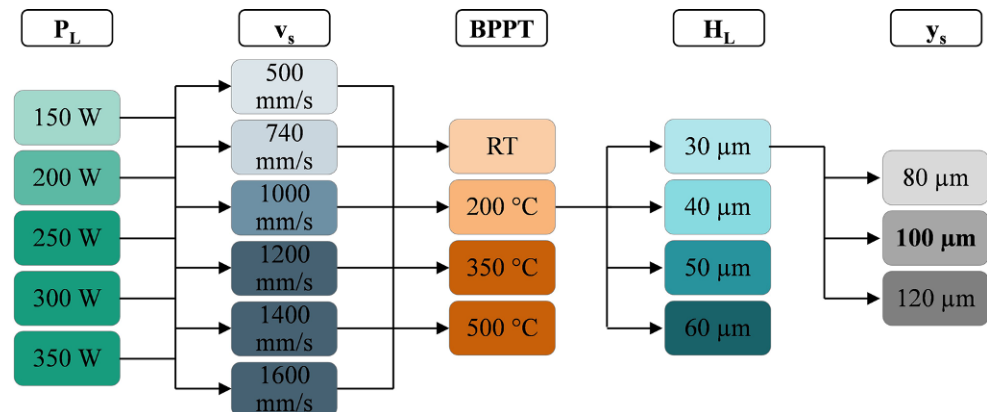
In the experiments, cube-shaped test specimens with a dimension of 10 × 10 × 10 mm³ were produced, using a zig-zag pattern with an alternating hatch rotation of 90° per layer as an exposure strategy. The feed direction of the laser is always turned 45° against the shielding gas flow. The specimens are arranged in a grid on the build plate, and the process parameters are randomly assigned to the individual specimens. For different BPPTs used in the experiments, the preheating system was programmed to a heating ramp of 10 K/min for heat up and cool down after the build job.

The experiments were carried out using BPPTs of Room Temperature (RT), 200 °C, 350 °C, and 500 °C. For the experiments conducted under RT, no BPPT was set. Additionally, the process parameters laser power (P_L), scan speed (v_s), layer height (H_L) and hatch distance (y_s) were varied. The

TABLE 1
Chemical composition of HS2-2-2 by Erasteel GmbH [13]

Chemical Elements [wt.-%]	C	Si	Mn	Cr	Mo	W	V	Fe
HS2-2-2 (1.3397, ASP2012)	0.6	1.0	0.3	4.0	2.0	2.1	1.5	Balance

Fig. 1: Variation of the process parameters laser power (P_L), scan speed (v_s), preheating temperature (BPPT), layer height (H_L), and hatch distance (y_s)



overall variations of the different process parameters are shown in detail in Fig. 1.

After manufacturing, the specimens were cut from the substrate plate using electrical discharge machining (EDM) wire cutting and then cut perpendicular to the melt tracks of the topmost layer using a wet cutting machine. The specimens are then ground and polished with 1 μm diamond suspension. The resulting cross-sections were then examined by light optical microscopy (LOM) using the microscope Olympus BX53M from Carl Zeiss Microscopy GmbH. The microscopy images were also used to determine the relative density and the ratio of the measured total crack area to the reference measured area (CAA). Selected cross-sections were etched with 10% aqueous nitric acid to reveal the microstructure and to determine the melt pool dimensions in the topmost layer. The melt pool width (MPW) and the melt pool depth (MPD) were then used to determine the melt pool area (MPA). For this purpose, axisymmetric melt pools were assumed, whose area was approximated with a triangle.

3. Results and Discussion

Figure 2 shows the relative density of all specimens built up with the parameters given in Fig. 1 over the volume energy (E_v). Vertical dashed lines indicate a volume energy range from 40 to 75 J/mm³ and horizontal dashed lines indicate a relative density of 99.50%. The specimens shown in graphs a) to d) were built with $H_L = 30 \mu\text{m}$ and with BPPT = RT, 200 °C, 350 °C, and 500 °C. The specimens shown in the graphs e) to g) were built with BPPT = 200 °C and with $H_L = 30 \mu\text{m}$, 40 μm, 50 μm, and 60 μm. Graph b) includes specimens built with $y_s = 80 \mu\text{m}$, 100 μm, and 120 μm. For all other specimens, $y_s = 100 \mu\text{m}$ was used.

The results shown indicate that relative densities of more than 99.50% can be achieved in a volume energy range from approx. 40 J/mm³ to approx. 75 J/mm³ over all BPPTs, H_L and y_s . Except for the specimens built with $H_L = 60 \mu\text{m}$, relative densities of more than 99.90% can be achieved in multiple specimens in all experiments. For specimens in a volume energy range from 75 to 175 J/mm³, an increasing scattering of the measured relative densities

Fig. 2: Relative density over E_v for $H_L = 30 \mu\text{m}$, 40 μm, 50 μm, 60 μm and BPPT = RT, 200 °C, 350 °C, 500 °C

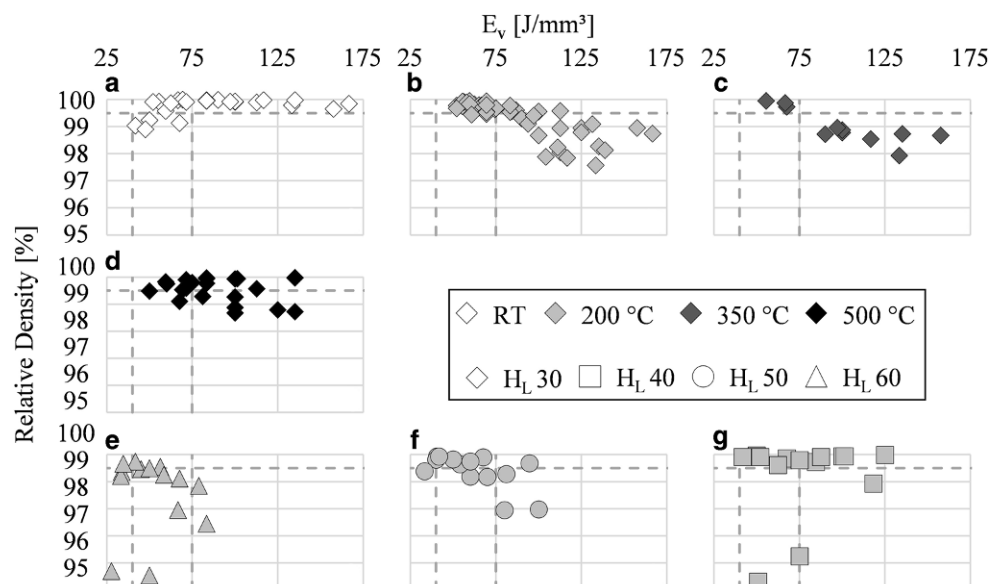
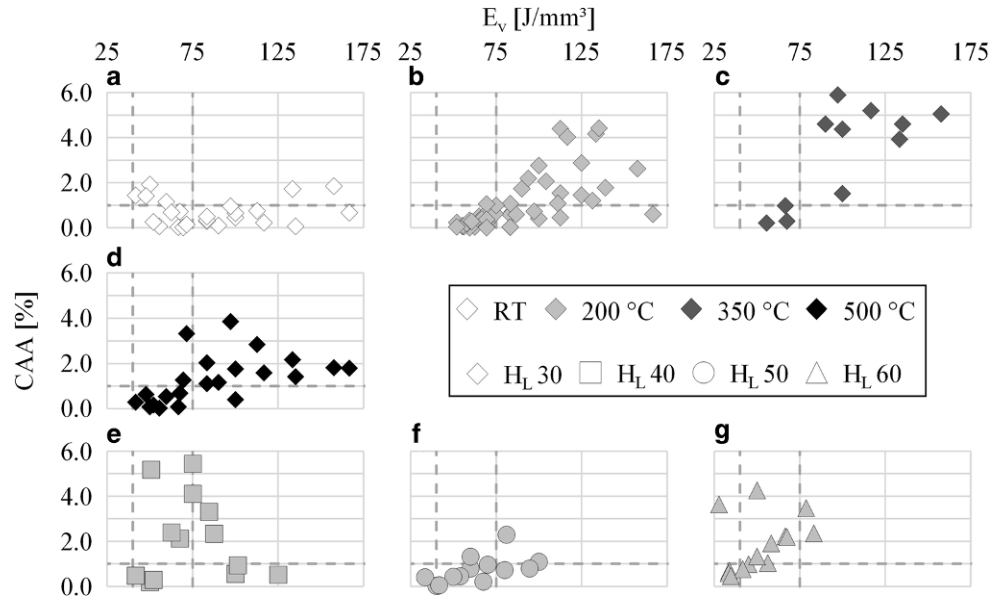


Fig. 3: CAA over E_v for $H_L=30\mu\text{m}, 40\mu\text{m}, 50\mu\text{m}, 60\mu\text{m}$ and BPPT = RT, 200 °C, 350 °C, 500 °C



can be observed. For volume energies below 30J/mm^3 and above 175J/mm^3 no specimens with a relative density above 99.50% could be produced. Specimens built at BPPT = RT show densities of 99.50% for the most part. However, large cold cracks were found in many of these specimens.

Figure 3 shows the evaluation of hot cracks as CAA over the E_v for the same specimens displayed in Fig. 2. The assignment of the specimens to the graphs also corresponds to Fig. 2. Here, vertical dashed lines indicate a volume energy range from 40 to 75J/mm^3 and horizontal dashed lines indicate a CAA of 1%.

Specimens built at room temperature partly show macroscopic cracks in the form of cold cracks. These cold cracks are not included in the evaluation of the hot cracks and therefore do not influence the CAA value. Specimens built with BPPT = 200 °C and above do not exhibit this kind of cold cracks anymore. With increasing volume energy, the CAA value increases across all experiments. In addition, a greater scattering of the measured values can be observed with increasing volume energy. In a volume energy range of 40 to 75J/mm^3 , the smallest average CAA

value of $0.28\% \pm 0.26\%$ can be measured for specimens built with BPPT = 200 °C and $H_L=30\mu\text{m}$. The largest average CAA value of $2.52\% \pm 2.02\%$ occurs for specimens built with BPPT = 200 °C and $H_L=40\mu\text{m}$. The smallest overall CAA value with a value of 0.0185% is measured for specimens built with $y_s=80\mu\text{m}$, BPPT = 200 °C, and $H_L=30\mu\text{m}$. Specimens manufactured at BPPT = 350 °C with $H_L=30\mu\text{m}$ show the highest total CAA values of up to 5.90%. The reason for the mostly low CAA values in specimens with $H_L=50\mu\text{m}$ has yet to be determined.

Figure 4 shows the MPD (a) and MPW (b) over E_v for all experiments conducted. The results show that both the width and depth of the melt pools increase with increasing E_v . For specimens manufactured with $H_L=30\mu\text{m}$, the average MPD and MPW in an E_v range between 40 and 75J/mm^3 are $110\mu\text{m} \pm 20\mu\text{m}$ and $137\mu\text{m} \pm 22\mu\text{m}$ respectively.

Figure 5 shows the overall variation of the resulting MPA over E_v (a) and CAA over MPA (b) for BPPTs from RT to 500 °C and H_L s from 30 to $60\mu\text{m}$. In Fig. 5a vertical dashed lines mark an E_v range from 40 to 75J/mm^3 , while the horizontal dashed lines mark an MPA range from 0.004mm^2 to 0.012mm^2 . In Fig. 5b vertical dashed lines mark an MPA

Fig. 4: (a) MPD over E_v and (b) MPW over E_v for $H_L=30\mu\text{m}, 40\mu\text{m}, 50\mu\text{m}, 60\mu\text{m}$ and BPPT = RT, 200 °C, 350 °C, 500 °C

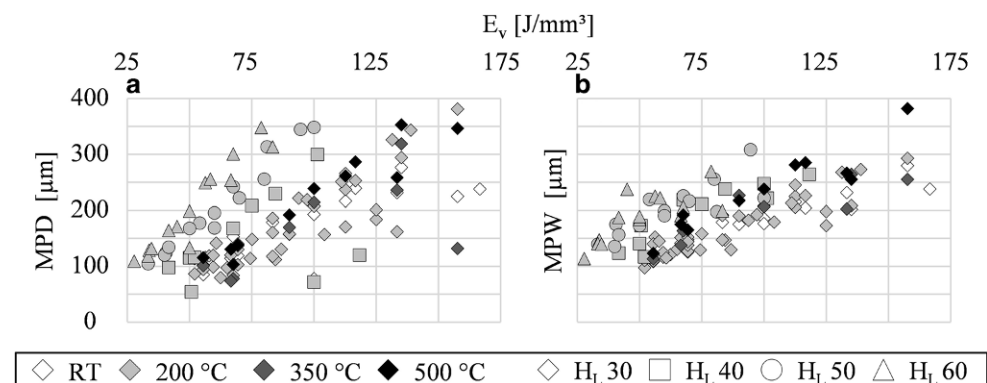
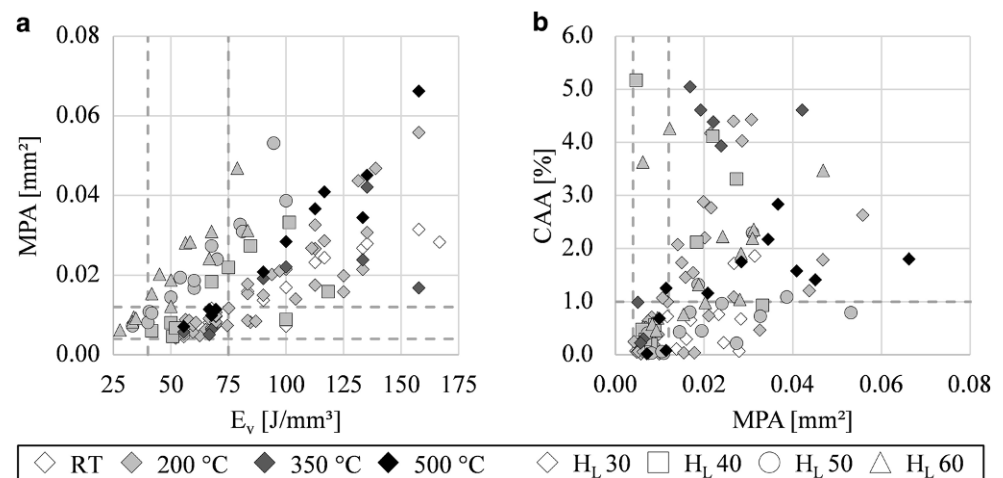


Fig. 5: **a** MPA over E_v and **(b)** CAA over MPA for $H_L = 30 \mu\text{m}$, $40 \mu\text{m}$, $50 \mu\text{m}$, $60 \mu\text{m}$ and BPPT = RT, 200°C , 350°C , 500°C



range from 0.004 mm^2 to 0.012 mm^2 , while the horizontal dashed line marks a CAA value of 1%.

The results displayed in Fig. 5a show an increasing MPA with increasing E_v . In the E_v range of 40 to 75 J/mm^3 described above, MPAs of up to 0.03 mm^2 are produced across all process parameters. For $E_v > 75 \text{ J/mm}^3$ a greater scattering of the measured values is observed. MPAs smaller than 0.004 mm^2 generally do not occur. Taking the results from Fig. 4 into account, this shows that narrow and shallow melt pools are formed at lower E_v and wider and deeper melt pools are formed at higher E_v . Figure 5b shows that larger MPAs tend to lead to larger CAAs. MPAs up to 0.012 mm^2 produce CAA values below 1% across all process parameters with only a few exceptions. In these exceptional cases, large-scale tethering errors with adjacent cracks were found to affect the measured CAA. This boundary partially also applies for MPA greater than 0.012 mm^2 , but a greater scattering of the measured values is observed here. These re-

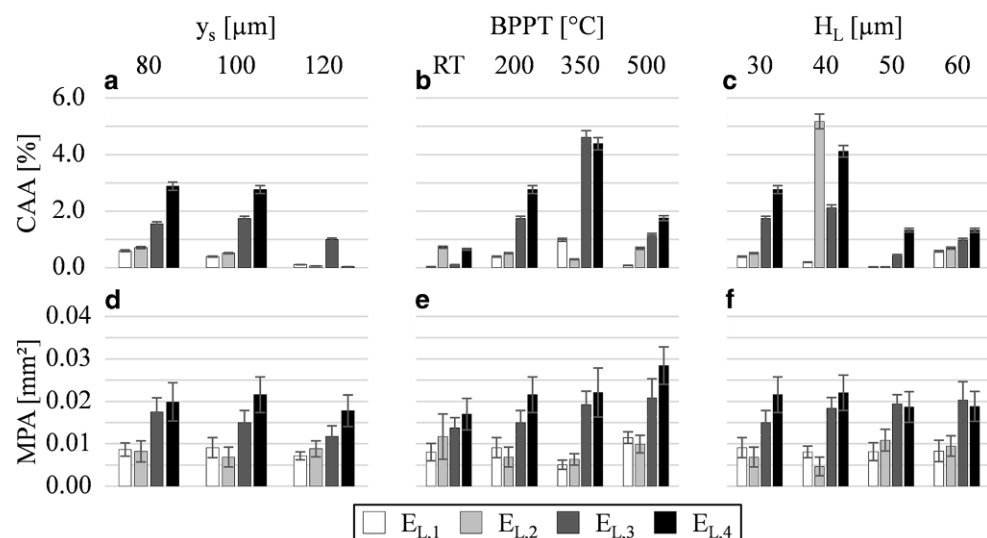
sults show that the CAA decreases with a smaller MPA and thus narrower and shallower melt pools.

Since the volume energy combines several process parameters (P_L , v_s , H_L , γ_s), the influences of these parameters are examined individually in more detail in the following. Figure 6 shows the CAA and MPA over γ_s , BPPT and H_L for four different line energies (E_L) ascending from left to right within a bar group with $E_{L,1} = 0.2 \text{ J/mm}$, $E_{L,2} = 0.203 \text{ J/mm}$, $E_{L,3} = 0.27 \text{ J/mm}$ and $E_{L,4} = 0.3 \text{ J/mm}$.

The specimens in Fig. 6a and b were produced with BPPT = 200°C and $H_L = 30 \mu\text{m}$. For the specimens of Fig. 6c and d, $H_L = 30 \mu\text{m}$ and $\gamma_s = 100 \mu\text{m}$ were used. The specimens in Fig. 6e and f were produced with BPPT = 200°C and $\gamma_s = 100 \mu\text{m}$.

Figure 6a, c and e show that the investigated process parameters γ_s , BPPT, and H_L have a separate influence on the CAA value. On average, a decrease in the CAA with increasing γ_s can be observed. However, for 80 and $100 \mu\text{m}$, a larger

Fig. 6: CAA and MPA over γ_s , BPPT and H_L for $E_{L,1}$ – $E_{L,4}$



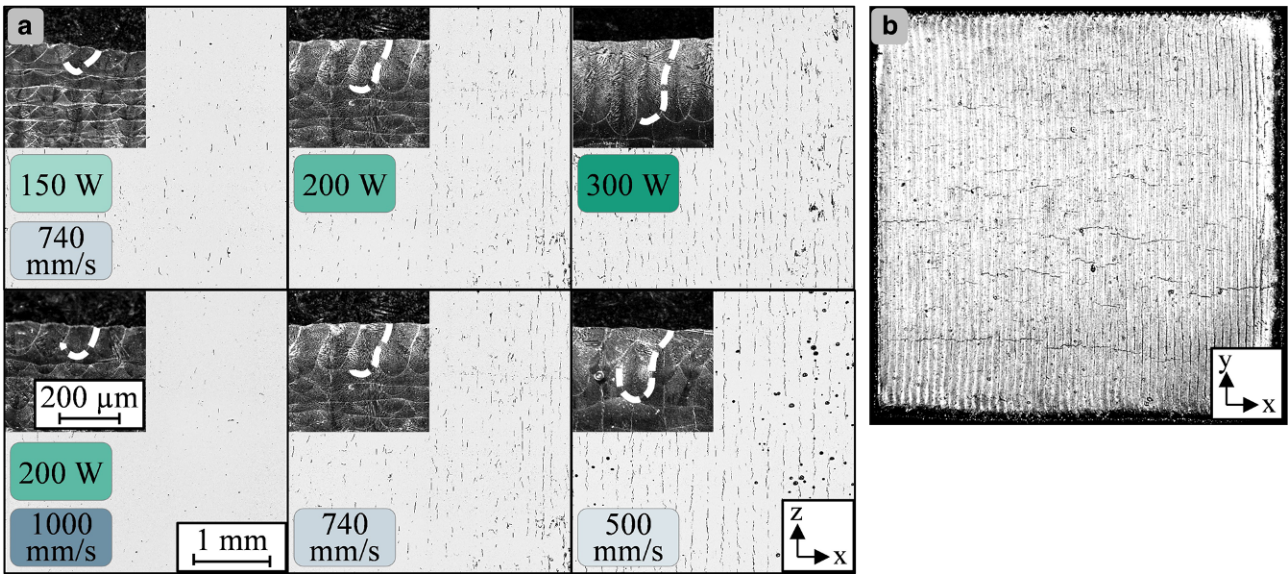


Fig. 7: **a** Cross-section and melt pool shape of specimens built at BPPT = 200 °C with different laser powers and scan speeds and **(b)** top view of the topmost layer of a specimen built at BPPT = 200 °C with $P_L = 300$ W and $v_s = 740$ mm/s

difference in the CAA values can be observed with increasing E_L . At 120 µm, comparatively small CAA values are measured. The preheating temperature (Fig. 6c) is shown to have a significant influence on the CAA value, which is even larger than the influence of the different E_L . The highest CAA values are measured at BPPT = 350 °C, whereas the lowest CAA values are measured at BPPT = RT. Similarly, with a variation of H_L (Fig. 6e, f), where the highest CAA values are measured at $H_L = 40$ µm while the lowest CAA values are measured at $H_L = 50$ µm.

Figure 6b shows that the hatch distance does not seem to have a significant influence on the MPA, here the difference in E_L predominates. In contrast, in Fig. 6d, the MPA tends to increase with increasing BPPT. Figure 6f shows that although the MPA increases with increasing E_L , it does not show larger deviations with constant E_L over all layer heights.

Figure 7a shows cross-sections of six specimens built at BPPT = 200 °C and an etched segment of the topmost layers of each specimen. The melt pool boundary of individual melt pools is highlighted by a dashed line. The cross-sections shown are parallel to the buildup direction z, as

indicated. The first three specimens are fabricated with $v_s = 740$ mm/s and with $P_L = 150$ W, 200 W, and 300 W. The remaining three specimens are fabricated with $P_L = 200$ W and with $v_s = 500$ mm/s, 740 mm/s, and 1000 mm/s.

For all variations of P_L and v_s cracks occur within the specimens. As P_L is increased, so does the number and the area of the cracks. The same is observed with decreasing scan speed. Therefore, an increase in the number and size of the cracks can be observed with an increasing line energy. However, the morphology of the cracks remains largely the same. All cracks appear at periodic intervals along the x-axis running parallel to the buildup direction z. As the number increases, cracks increasingly line up in rows. As indicated through the white dashed lines the shape and size of the melt pool also change with line energy. It seems to be irrelevant for the size of the melt pools whether E_L is controlled by a change of v_s or P_L . However, the shape of the melt pools shown seems to change from a drop-like shape for larger E_L to an elliptical shape for smaller E_L when v_s is adjusted at constant P_L . When P_L is adjusted at constant v_s , the drop shape seems to be maintained.

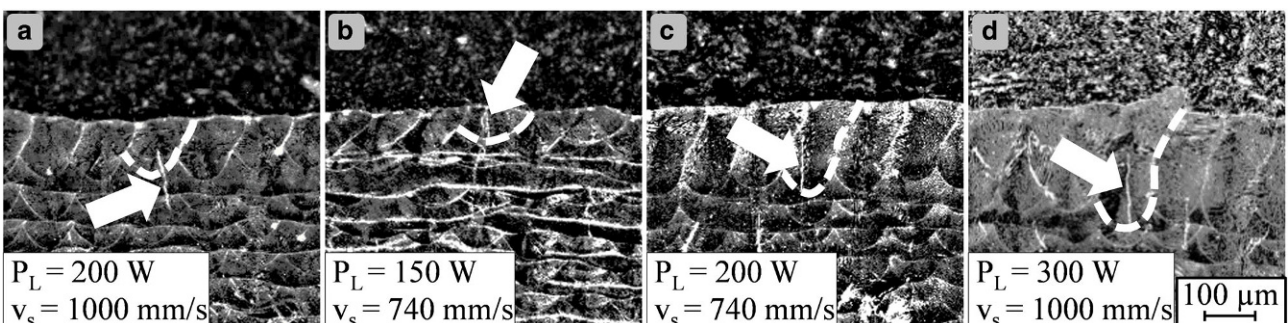


Fig. 8: Etched cross-section of four specimen $E_{L,1}$, $E_{L,2}$, $E_{L,3}$ and $E_{L,4}$ built with BPPT = 200 °C with cracks running through individual melt pools

Fig. 9: Melt pools of specimens built with BPPT = 200 °C and $v_s = 100 \mu\text{m/s}$; a with $E_L = 0.47 \text{ J/mm}$ and average MPA = 0.056 mm^2 ; b detail of the crack from a and c with $E_L = 0.17 \text{ J/mm}$ and average MPA = 0.006 mm^2

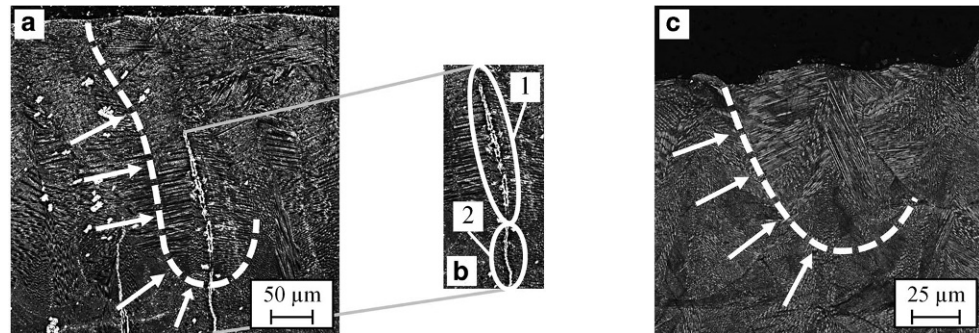


Figure 7b shows the topmost layer of the specimen built with BPPT = 200 °C, $P_L = 300 \text{ W}$, and $v_s = 740 \text{ mm/s}$ before cutting. It is noticeable that the visible cracks run perpendicular to the melt tracks in the x-direction. This contradicts the expectation, based on the cross-sections in a), that the hot cracks run parallel to the melt tracks. This could be due to cracks developed in adjacent lower layers continuing at the surface. As can be seen in a), the cracks in the cross-sections seem to run partly across several layers, which supports this assumption.

Figure 8 shows the etched cross-sections of the last layer of four different specimens prepared with parameters that yield ascending line energies corresponding to the ones described above. The melt pool boundary containing a crack is highlighted by a dashed line for each individual specimen. The melt pools vary in width and depth as well as in the melt pool shape, which ranges from elliptical to drop-shaped. All highlighted melt pools are intersected by a crack in the center. The paths of the cracks vary. In Fig. 8a, the crack starts in the center of the melt pool and runs into the adjacent layers below it. In Fig. 8b, the crack divides the melt pool vertically and stops at the melt pool boundary. The crack therefore does not connect to other visible cracks in the adjacent layer below that connects to the same melt pool boundary. In Fig. 8c,d, the crack starts in the center of the melt pool and ends at the boundary of the melt pool.

Figure 9 shows detailed LOM pictures of two melt pools from specimens with $E_L = 0.47 \text{ J/mm}$ and $E_L = 0.17 \text{ J/mm}$ respectively.

For the specimen from Fig. 9a, an average MPA of 0.056 mm^2 is measured. The arrows indicate the orthogonal growth direction of the dendrites from the melt pool edge. Dendrites along the steep melt pool flank are almost parallel oriented to each other and grow toward the center of the melt pool. A crack has formed between the solidification fronts that have been created (Fig. 9b, Sect. 1). This upper part of the crack is orthogonal to the dendrites and has rather irregular crack edges, leading to the assumption that it might be a solidification crack. The lower part of the crack shown in Sect. 2, on the other hand, has sharp crack edges, suggesting that it could be a cold crack initiated from the hot crack above. The underlying mechanism here is assumed to be the stresses that arise during the solidification of the dendrites due to shrinkage against the direction of solidification. The melt pool shown in Fig. 9c, with an average MPA of 0.006 mm^2 also shows dendrites growing orthogonal to the melt pool edge. In contrast to

a), the dendrites meet here at various angles, which can be attributed to the absence of steep melt pool edges as can be observed for a).

4. Conclusion

In this contribution, the occurrence of hot cracks during the processing of HS2-2-2 by LPBF was investigated with a variation of the process parameters laser power, scan speed, hatch distance, layer height, and build plate preheating temperature. Two different types of cracks were found in the cross-sections of the manufactured specimens. Large cracks have occurred isolated without preferential direction. These are identified as cold cracks based on their course and shape. In addition, periodic microcracks with a clear preferred direction along the buildup direction have been detected in almost all specimens. The melt pool analysis has shown that these cracks are preferentially found in the center of individual melt pools, hence the cracks are identified as hot cracks or specifically as solidification cracks.

Density evaluations show that specimens with a relative density of 99.5% can be produced at a volume energy range of 40 to 75 J/mm^3 . In addition, cold cracks can be prevented with a preheating temperature of 200 °C or more. Furthermore, it can be shown that the shape and size of the melt pools are dependent on the volume energy; larger volume energies therefore tend to produce larger melt pool widths and depths.

The analysis of the influences of the process parameters laser power, scan speed, hatch distance, layer height, and preheating temperature on crack formation has shown that the laser power and scan speed, hence the line energy, have the largest influence on the melt pool shape and size as well as the crack formation. Smaller line energies lead to decreasing melt pool widths and depths and thus smaller melt pool areas. This is due to the fact that higher energy inputs trigger deep-welding effects, while heat conduction welding effects increasingly come into play at lower energy inputs. These heat conduction welding effects produce rather elliptical melt pool shapes instead of drop-like melt pool shapes as is the case for the deep welding effects. The steep flanks of the drop-shaped melt pools, which run almost orthogonally to the build platform, favor the growth of dendrites from the side walls to the center axis of the melt pools, which in turn favors the formation of hot cracks

in the form of solidification cracks along the center axis of the melt pools. In the elliptical melt pools, these steep melt pool flanks do not occur which leads to a growth of the dendrites under various angles with a decreased formation of hot cracks. From this, it can be concluded that hot crack formation can be controlled primarily by the shape of the melt pools. It was shown that a change of the melt pool shape from a drop shape to an elliptical shape can rather be achieved by adjusting the scan speed.

Furthermore, it is shown that the formation of hot cracks can already be reduced without the use of a preheating system but peaks at a build plate preheating temperature of 350 °C. For the different layer heights, no correlations could be derived. However, for a layer height of 50 µm, higher densities and lower CAA values are measured throughout.

The combined influences of the investigated process parameters on the melt pool shapes and sizes and thus the formation of hot cracks remain to be investigated. A more in-depth classification of the observed cracks by examining the microstructure also remains to be done.

Acknowledgements. This project was carried out with the support of the Aachen Center for Additive Manufacturing (ACAM) and associated industrial partners.

Funding. Open Access funding enabled and organized by Projekt DEAL.

Open Access This article is licensed under a Creative Commons Attribution 4.0 International License, which permits use, sharing, adaptation, distribution and reproduction in any medium or format, as long as you give appropriate credit to the original author(s) and the source, provide a link to the Creative Commons licence, and indicate if changes were made. The images or other third party material in this article are included in the article's Creative Commons licence, unless indicated otherwise in a credit line to the material. If material is not included in the article's Creative Commons licence and your intended use is not permitted by statutory regulation or exceeds the permitted use, you will need to obtain permission directly from the copyright holder. To view a copy of this licence, visit <http://creativecommons.org/licenses/by/4.0/>.

References

1. Ahn, D.-G.: Applications of laser assisted metal rapid tooling process to manufacture of molding & forming tools – state of the art. *Int. J. Precis. Eng. Manuf.* **12**(5), 925–938 (2011)
2. Blakey-Milner, B., Gradl, P., Snedden, G., Brooks, M., Pitot, J., Lopez, E., Leary, M., Berto, F., Du Plessis, A.: Metal additive manufacturing in aerospace: A review. *Mater. Des.* **209**, 110008 (2021)
3. Saewe, J., Carstensen, N., Kürsteiner, P., Jägle, E.A., Schleifenbaum, J.H.: Influence of increased carbon content on the processability of high-speed steel HS6-5-3-8 by laser powder bed fusion. *Addit. Manuf.* **46**, 102125 (2021)
4. Narasimharaju, S.R., Zeng, W., See, T.L., Zhu, Z., Scott, P., Jiang, X., Lou, S.: A comprehensive review on laser powder bed fusion of steels: Processing, microstructure, defects and control methods, mechanical properties, current challenges and future trends. *J Manuf Process* **75**, 375–414 (2022)
5. Saewe, J.: Untersuchungen der Verarbeitbarkeit des Schnellarbeitsstahls HS6-5-3-8 mittels Laser Powder Bed Fusion, 1st edn. Apprimus, Aachen (2022)
6. Saewe, J., Gayer, C., Vogelpoth, A., Schleifenbaum, J.H.: Feasibility investigation for laser powder bed fusion of high-speed steel AISI M50 with base preheating system. *Berg. Huettenmaenn. Monatsh.* **164**(3), 101–107 (2019)
7. Bargel, H.-J., Schulze, G. (eds.): *Werkstoffkunde*, 11th edn. Springer, Berlin, Heidelberg (2012)
8. Sander, J.: *Selektives Laserschmelzen hochfester Werkzeugstähle*, Dissertation, Technische Universität Dresden, Dresden (2018)
9. Saewe, J., Wilms, M.B., Jauer, L., Schleifenbaum, J.H.: Influence of preheating temperature on hardness and microstructure of high-speed steel HS6-5-3-8 manufactured by laser powder bed fusion. In: *Metal Additive Manufacturing Conference (MAMC)* (2019)
10. Vrancken, B.: *Study of Residual Stresses in Selective Laser Melting* (2016)
11. Kou, S.: *Welding Metallurgy*, 3rd edn. Wiley, Hoboken (2021)
12. Krafka, H.: Risse in Schweißverbindungen – Heißrissarten, Heißrissentstehung und Heißrissprüfung. In: *DVM-Bericht Festigkeits- und Bruchverhalten von Fügeverbindungen*, pp. 161–171. DVM – Deutscher Verband für Materialforschung und -prüfung, (2000)
13. Vario Edelstahl AG (ed.): *Werkstoffdatenblatt ASP 2012 Hochzäh "Gummistahl" PM-Hochleistungs-Stahl*. <https://www.varioedelstahl.ch/wp-content/uploads/2020/04/ASP-2012.pdf>, Accessed 3 Aug 2022

Publisher's Note. Springer Nature remains neutral with regard to jurisdictional claims in published maps and institutional affiliations.